California Solar Initiative

RD&D: Research, Development, Demonstration and Deployment Program

GO solar CALIFORNIA

Final Project Report:

Comprehensive Grid Integration of Solar Power for SDG&E

Grantee:

University of San Diego

October 2016

www.CalSolarResearch.ca.gov

PREPARED BY

UC San Diego

9500 Gilman Drive
La Jolla, CA 92093-0411

Principal Investigators:

Jan Kleissl
jkleissl @ ucsd.edu
858-534-8087
Dept of Mechanical & Aerospace Engineering
Center for Renewable Resources &Integration and the Center for Energy Research

Project Partners:

San Diego Gas & Electric and Vertum Partners

PREPARED FOR

California Public Utilities Commission
California Solar Initiative: Research, Development, Demonstration, and Deployment Program

CSI RD&D PROGRAM MANAGER

Itron CSI RD&D Program Manager

Program Manager:
Smita Gupta
Smita.Gupta @ itron.com
509-891-3189

Project Manager:
Stephan Barsun
stephan.barsun @ itron.com
509-891-3193

Additional information and links to project related documents can be found at *http://www.calsolarresearch.ca.gov/Funded-Projects/*

Preface

The goal of the California Solar Initiative (CSI) Research, Development, Demonstration, and Deployment (RD&D) Program is to foster a sustainable and self-supporting customer-sited solar market. To achieve this, the California Legislature authorized the California Public Utilities Commission (CPUC) to allocate **$50 million** of the CSI budget to an RD&D program. Strategically, the RD&D program seeks to leverage cost-sharing funds from other state, federal and private research entities, and targets activities across these four stages:

- Grid integration, storage, and metering: 50-65%
- Production technologies: 10-25%
- Business development and deployment: 10-20%
- Integration of energy efficiency, demand response, and storage with photovoltaics (PV)

There are seven key principles that guide the CSI RD&D Program:

1. **Improve the economics of solar technologies** by reducing technology costs and increasing system performance;
2. **Focus on issues that directly benefit California**, and that may not be funded by others;
3. **Fill knowledge gaps** to enable successful, wide-scale deployment of solar distributed generation technologies;
4. **Overcome significant barriers** to technology adoption;
5. **Take advantage of California's wealth of data** from past, current, and future installations to fulfill the above;
6. **Provide bridge funding** to help promising solar technologies transition from a pre-commercial state to full commercial viability; and
7. **Support efforts to address the integration of distributed solar power into the grid** in order to maximize its value to California ratepayers.

For more information about the CSI RD&D Program, please visit the program web site at www.calsolarresearch.ca.gov.

Abstract

The University of California, San Diego (UC San Diego) and its partners demonstrated forecasting and solar power integration tools to support the goals of the California Public Utilities Commission's California Solar Initiative (CSI) Research, Development, Demonstration and Deployment Program (CSI RD&D). This project demonstrated solar forecasting models and battery energy storage system (BESS) siting and operation models to facilitate PV grid integration. This work focused on a San Diego Gas & Electric (SDG&E), a California utility dealing with high PV penetration.

Operational solar and net load forecasting systems were demonstrated for SDG&E. The purpose of the solar forecast system was to provide solar generation inputs into system-wide net load forecasts and operational load flow analysis. A numerical weather prediction atmospheric modeling system for coastal Southern California was implemented and post-processing was applied to improve forecast accuracy. The solar forecast system has been operational since May 2015 at high reliability and is expected to remain operational past the end of this grant project.

Net load forecasting was demonstrated for 68 substations and validated for forecast horizons ranging from 10 min to 4 days. Stochastic learning methods such as Artificial Neural Networks (ANN), and Support Vector Regression (SVR) are trained on sky images and substation net load data. Stochastic-learning models significantly outperform the reference persistence forecast model. These models were assembled into forecasting packages that are operational with real-time telemetry data.

The main thrust of the project was improving distribution feeder power quality under high PV penetration utilize BESS. UC San Diego conducted power flow simulations for 14 representative SDG&E feeders with high PV penetration to quantify voltage variations, overvoltage conditions, and load tap changer operations connected to solar power variability. Voltage profiles along each feeder together with the thermal rating of electrical conductors informed an algorithm that identified feeder hotspots arising from both solar variability and feeder stress. The results of the case study highlighted that significant increases in PV penetration levels across all of the 14 feeders are feasible without network augmentation. BESS can further increase high PV penetration, but the ideal siting is a practical challenge. A methodology for optimal allocation of BESS sizes to maximize their support for integrating high penetration PV in residential distribution networks and minimize cost was developed and demonstrated. The algorithm is available for use by other researchers and industry. The effectiveness of the proposed method was demonstrated on the IEEE 8500-Node test feeder and a feeder in the SDG&E service area. Finally a way to leverage phasor measurement units for grid disturbance detection, modeling, and actuation using BESS was demonstrated.

Contents

Executive Summary

The University of California, San Diego (UC San Diego) and its partners improved and demonstrated forecasting and solar power integration tools to support the goals of the California Public Utilities Commission California Solar Initiative (CSI) Research Development, Demonstration and Deployment Program (RD&D). This final report provides a summary of work done under this grant and more detailed results can be found in the individual deliverables.

Operational solar and net load forecasting systems were demonstrated for SDG&E. The purpose of the solar forecast system was to provide solar generation inputs into system-wide net load forecasts and operational load flow analysis. A numerical weather prediction atmospheric modeling system for coastal Southern California was implemented and post-processing was applied to improve forecast accuracy. The solar forecast system has been operational since May 2015 at high reliability and is expected to remain operational past the end of this grant project. Data assimilation improved the forecast accuracy for a few sample days and will be integrated into the forecast system in the future.

Net load forecasting was demonstrated for 68 substations and validated for forecast horizons ranging from 10 min to 4 days. Stochastic learning methods such as Artificial Neural Networks (ANN), Support Vector Regression (SVR) are trained on sky images and substation net load data. Stochastic-learning models significantly outperform the reference persistence forecast model. For the relatively low solar penetration levels encountered at the feeders studied (2% and 6%), the availability of sky images reduced forecast errors only by about 5%. These models were assembled into forecasting packages that are operational with real-time telemetry data.

The main thrust of the project was improving distribution feeder power quality under high PV penetration utilize BESS. UC San Diego conducted power flow simulations for 14 representative SDG&E feeders with high PV penetration to quantify voltage variations, overvoltage conditions, and load tap changer operations. Voltage profiles along each feeder together with the thermal rating of electrical conductors informed an algorithm that identified feeder hotspots arising from both solar variability and feeder stress (Figure ES-1). The results of the case study highlighted that significant increases in PV penetration levels across all of the 14 feeders are feasible without network augmentation.

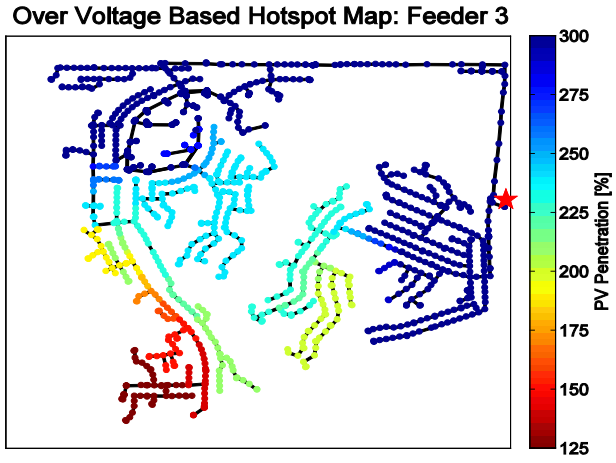

Figure ES-1: Hotspot map for a sample feeder. The star indicates the distribution substation. The color bar indicates PV penetration levels that correspond to a thermal over-load (line color) and/or voltage exceedance (symbol).

Further, the increase in PV penetration levels varied based on the feeder topology. Feeder hotspots associated with the lowest PV penetration level were typically observed towards the end of a distribution feeder and/or along small branches of the feeder that did not carry the trunk sectional load. In all cases PV units were located at these respective hotspots. Consequently, PV generation sites closer to the trunk sectional load where the conductor has been sufficiently rated would improve the hosting capacity in most cases.

BESS can resolve hotspot issues and further increase high PV penetration, but the ideal siting is a practical challenge. A methodology for optimal allocation and sizing of BESS to maximize their support for integrating high penetration PV in residential distribution networks and minimize cost was developed and demonstrated. The effectiveness of the proposed method was demonstrated on the IEEE 8500-Node test feeder and a feeder in the SDG&E service area (Figure ES-2). The algorithm is available for use by other researchers and industry.

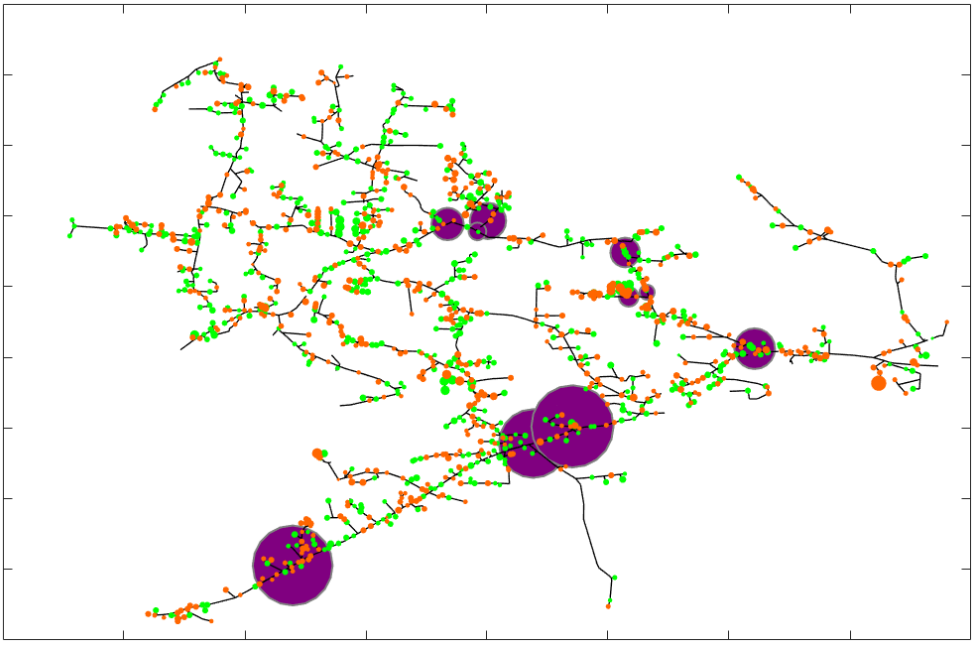

Figure ES-2: Optimal BESS solution on top of the one-line diagram of the IEEE8500 feeder. Locations of proposed BESS units are marked with purple dots. Orange dots show loads with PV and green dots show load points without PV. Each dot is sized with respect to the capacity of the component it is representing.

Finally a way to leverage phasor measurement units (PMU) for grid disturbance detection, modeling, and actuation using BESS was demonstrated. The effectiveness of the approach illustrating both the realization algorithm and the control methodology are illustrated on the measurements obtained from a three phase network where the power oscillation frequency and model order is known and used for comparison and validation of the method. The approach shows how the power oscillation frequency can be recovered from the real-time measurements and reduced with the proposed control algorithm very effectively. The approach shows a close connection between modeling power flow dynamics from disturbance data and data-based models (Figure ES-3) and in turn using those models for control design to mitigate electric power oscillations that exploit the fast dynamics and response time of modern BESS or PV inverters. The software for both event detection and modeling of the power flow dynamics has been bundled in a software package.

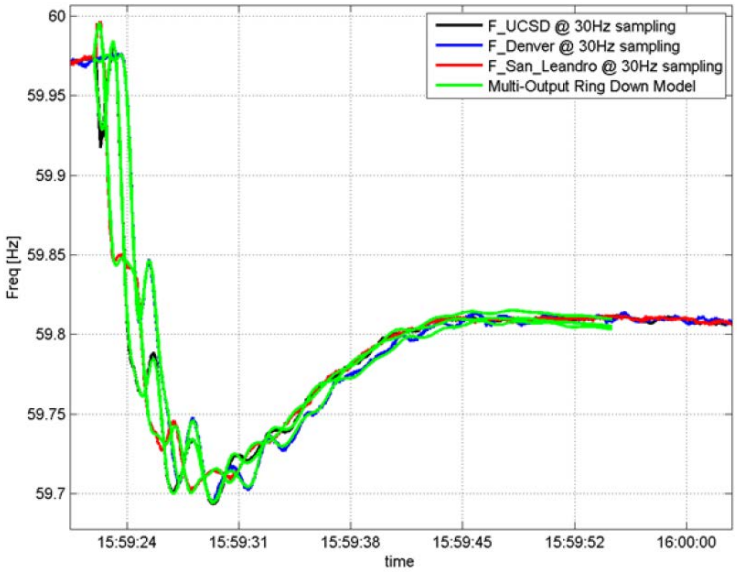

Figure ES-3: Comparison between PMU data and simulated data based on estimated discrete-time state space model for the analysis of a disturbance event. The frequency measurements from three different PMUs are used to quantify a detected event. The event was successfully resimulated as observed from a direct comparison with the measured time synchronized frequency measurements from the three different PMUs.

Acknowledgements

This work was supported by the California Solar Initiative RD&D program. We are grateful to Stephan Barsun, Itron for helpful comments, guidance, and for making connections with other CSI researchers. SolarAnywhere satellite solar resource data was provided by Clean Power Research.

1 Overview and Key Terms

The University of California, San Diego (UC San Diego) and its partners improved and demonstrated forecasting and solar power integration tools to support the goals of the California Public Utilities Commission California Solar Initiative (CSI). This final report provides a summary of work done under this grant and more detailed results can be found in the individual deliverables (see reference section).

Since several datasets and error metrics are common to different sections, Section 2 describes these data sets and equations. In particular, the SolarAnywhere satellite solar resource product and the SDG&E weather station network are described. PV penetration is defined. Further, bias error, absolute error, root mean square error, and forecast skill are defined.

In Section 3 an advanced operational ensemble solar forecast system is described. Numerical Weather Prediction (NWP) and statistical post-processing tools are applied to forecast solar irradiance across the SDG&E territory from hours to two days-ahead. Accuracy and reliability are quantified.

At the more granular level, net load forecasts for 68 SDG&E substation are described in Section 4. Forecast accuracy for horizons of 10 min to 4 days ahead are quantified. Sky imagery is used to improve the estimation of the solar power contribution to net load and including such data reduces forecast error.

Distribution feeder hotspots for 14 SDG&E feeders are visualized in Section 5 and an algorithm to site and size energy storage to reduce distribution feeder losses and voltage variability are described in Section 6. Finally, Section 7, describes a technique to use battery energy storage for damping transients and harmonics in the power grid.

Acronyms and Key Terms (see also NREL Glossary at http://rredc.nrel.gov/solar/glossary/)

3DVAR	3-dimensional variational data assimilation
AC	Alternating current. Typically used to characterize inverter capacity at a PV site.
DC	Direct current. Typically used to characterize PV panel capacity at a PV site.
DNI	Direct normal irradiance
FRoC	Filtered Rate of Change
GA	Genetic Algorithms
GHI	Global Horizontal Irradiance: sum of direct and diffuse irradiance on a horizontal surface.
GOES	Geostationary Operational Environmental Satellite
GTI	Grid-tied inverter
IOU	Investor-owned utilities (SDG&E, SCE, PG&E)
kt	Clear sky index: actual irradiance (or power output) normalized by expected clear sky irradiance or power output (Section 2.2).
MAE	Mean Absolute Error.
MBE	Mean Bias Error (Section 2.3)
NAM	North American Model
NWP	Numerical Weather Prediction

PG&E	Pacific Gas & Electric
PMU	Phasor Measurement Unit
PV	Photovoltaic
ρ	Correlation coefficient.
RMSE	Root Mean Square Error
SAW	SolarAnywhere satellite-derived solar resource data.
SBRA	Step-Based Realization Algorithm
SCE	Southern California Edison
SDG&E	San Diego Gas & Electric
SVR	Support Vector Regression
UTC	Universal Coordinated Time (PST = UTC – 8 hours).
WRF	Weather Research and Forecasting Model

2 Dataset and Error Metrics

2.1 Data

SolarAnywhere Satellite: Clean Power Research's commercially available SolarAnywhere (SAW) provides Global Horizontal Irradiation (GHI) and Direct Normal Irradiation (DNI) derived from Geostationary Operational Environmental Satellite (GOES) visible imagery at 30 minutes temporal and 1 km spatial resolution (Clean Power Research, 2014). To obtain GHI, a cloud index is calculated for each pixel from the reflectance measured by the satellite. Instantaneous, spatially averaged GHI is then calculated by using the cloud index along with a clear sky model that accounts for effects of turbidity.

Irradiance Sensors: Forecasts were also validated using GHI measurements operated by SDG&E. The measurement locations and their abbreviations are shown in Figure 1. The sites contain complete weather instrumentation including measurements of GHI by a Licor Li200 photodiode pyranometer at a temporal resolution of 10 minutes with an interval-ending time stamp.

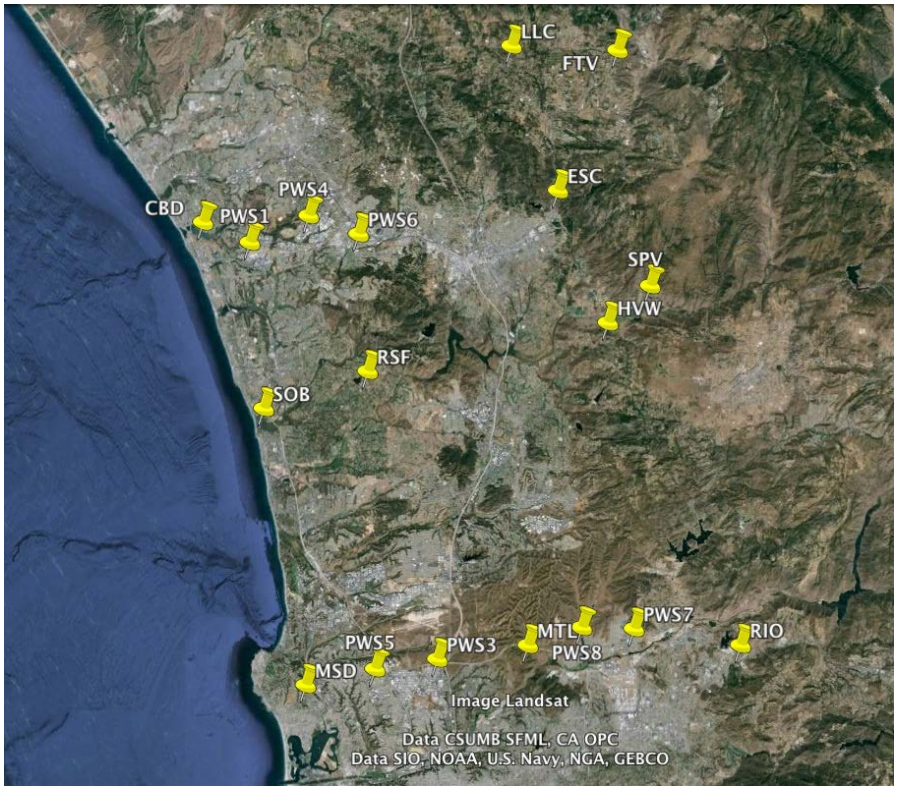

Figure 1: Irradiance Sensor measurement locations and their abbreviations. Locations and abbreviations for SGD&E weather stations can be found at Google Earth©.

2.2 PV penetration

PV penetration is defined as

$$PV\ penetration\ (\%) = \frac{P_{pv\_peak}}{P_{load\_peak}} \times 100\ \%,$$

where P_{pv_peak} is the cumulative rated AC power of all the PV systems, and P_{load_peak} the aggregated demand of all loads contributing to the feeder-level peak. A PV penetration level of 0% is equivalent to taking all PV units along a feeder out of service.

2.3 Error metrics

The main error metrics used within this report are Mean Absolute Error (MAE), Mean Bias Error (MBE) and Root Mean Square Error (RMSE). Furthermore, another metric called forecast skill was used to quantify the relative performance between two forecasts models. MAE is obtained by averaging the ***absolute value*** of the error, to give a measure of the accuracy of the predictions

$$MAE = \frac{1}{N}\sum_{i=1}^{N}|Prediction_i - Observation_i|$$

MBE is obtained by taking the ***straight average*** of the error values to give an idea if the prediction tends to be systematically higher or lower than the observation,

$$MBE = \frac{1}{N}\sum_{i=1}^{N}(Prediction_i - Observation_i)$$

RMSE is obtained by taking the average of the square of error values and taking the square root,

$$RMSE = \sqrt{\frac{1}{N}\sum_{i=1}^{N}(Prediction_i - Observation_i)^2}$$

Forecast Skill measures the performance of a forecast model with respect to a reference forecast, e.g. the performance of raw NWP or with respect to the persistence forecast. If there is no improvement, the forecast skill is 0. In the extreme case of perfect forecast, the forecast skill becomes 1.

$$\text{Forecast Skill} = 1 - \frac{RMSE_{Prediction}}{RMSE_{Reference}}$$

3 Advanced Operational Ensemble Solar Forecasting System

3.1 Solar forecast need and requirements

Solar forecasting is an important tool for power grid operations. Distributed solar power represents a negative load that negates some of the load on the distribution system. Knowledge of the resulting net load can help to operate the distribution system more efficiently, for instance in scheduling repairs, feeder switching, and emergency operations. San Diego Gas & Electric Company (SDG&E) is moving towards deep situational awareness on their distribution system. With rapid growth of solar PV in the SDG&E service territory, a solar forecast solution was desired.

For distribution system operations the primary time horizon of interest is intra-day forecasts. Forecasts were therefore generated for delivery prior to 0600 Pacific Time (PT = 1400 Universal Coordinated Time, UTC). The forecast horizon was 48 hours providing solar irradiance for the current and the following day at 15 min time steps. In this first operational implementation an intuitive quantity for solar intensity was desired. The Solar Potential Index is defined as the forecast global horizontal irradiance (GHI) divided by the peak global horizontal irradiance which would be expected at solar noon on the summer solstice (June 21) for a typical clear day. This normalized scale from 0 to 1 provides grid operators a better understanding of the relative importance of solar power generation on a particular day and hour.

Spatially, the SDG&E territory is divided into climate zones that map contiguous areas of similar solar resource. The solar potential index is averaged over all simulation grid cells located within a climate zone. While the SPI was used operationally, in this report solar forecasts of GHI are validated, which is a more commonly used metric to characterize the solar resource.

3.2 Solar forecast system

An open-source NWP model that is continuously updated by the National Center for Atmospheric Research (NCAR) is the Weather Research and Forecasting (WRF) model. Two one-way nested domains at 8.1 km and 2.7 km resolution were initialized at 12 UTC (= 0400 PT) in WRF version 3.6. Each domain contains 100 grid points in both horizontal directions and 75 vertical levels, with 50 levels below 3 km; their locations are shown in Figure 2. The time step was 10 sec and output was recorded at 15 min intervals.

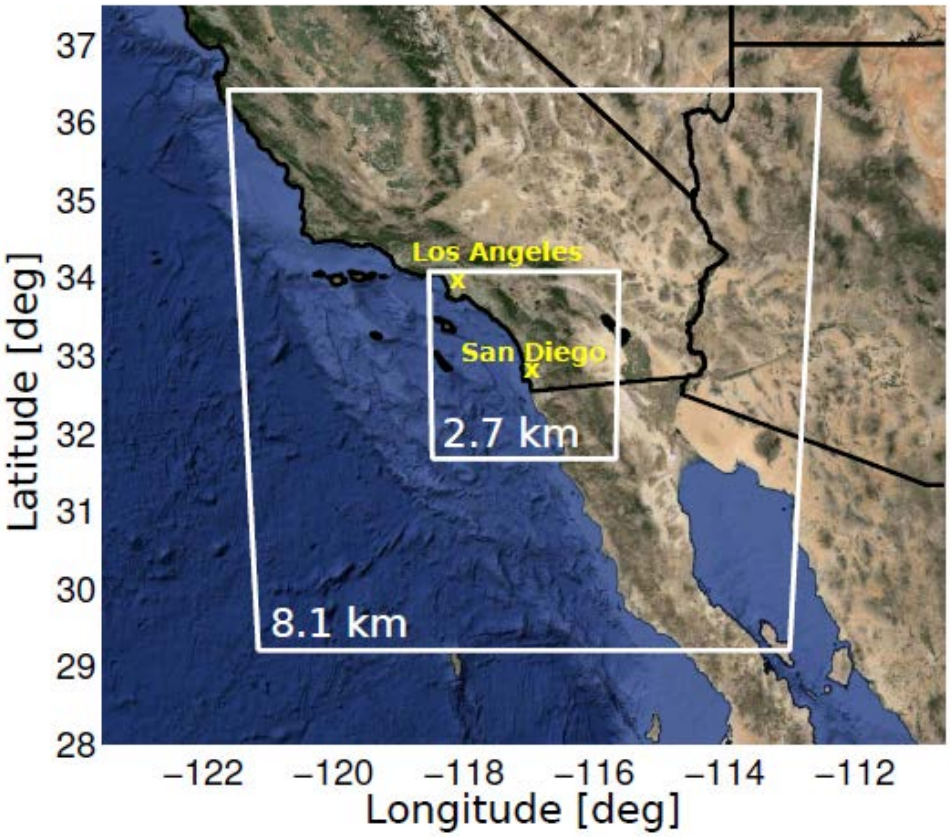

Figure 2: Outer and inner domains at 8.1 km (100x100x75 grid points) and 2.7 km (100x100x75) resolution. Satellite image © 2015 Google.

3.3 Validation results

The annual results show that the accuracy of the original WRF forecast is on par with persistence near the coast and superior further inland. The correction through an Analog Ensemble (AnEn) create a forecast that is superior to persistence everywhere. Monthly results indicate that the original WRF is superior to persistence during the winter when synoptic scale frontal systems dominate the weather conditions, while it is on par or slightly worse than persistence for the rest of the year.

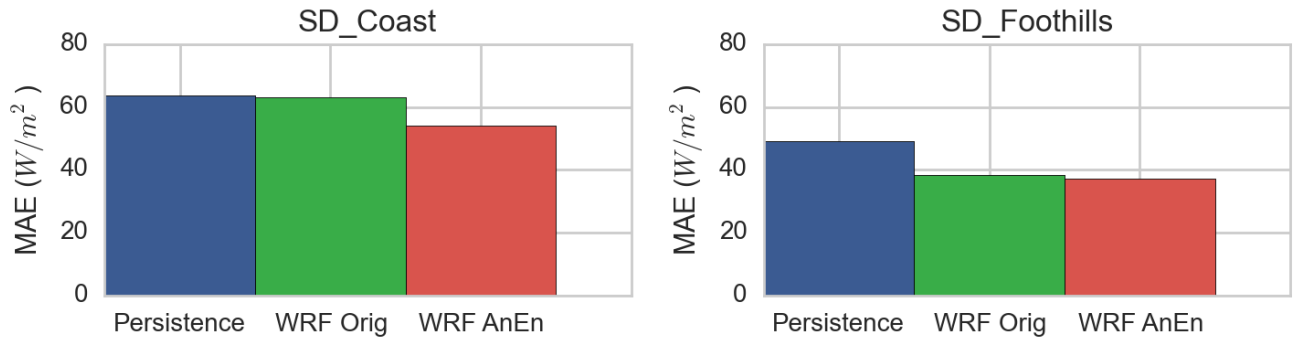

Figure 3: Mean Absolute Error for a coastal climate zone (left) and an inland climate zone (right) over one year of forecasting. WRF Orig is the raw WRF forecast and AnEn is the Analog Ensemble postprocessing.

3.4 Forecast improvements through data assimilation

The NAM parent model to the WRF provides the initial temperature and moisture fields. NAM underestimates the inversion base height and the liquid water content at model initialization, which reduces marine layer cloud formation under an otherwise suitable synoptic situation. Hence, improved solar forecasting requires improving the initial profiles of the prognostic variables.

3DVAR data assimilation uses observations from various sources and combines them with the short-range model forecast (called first guess) obtained from WRF simulation in order to provide the accurate state of the atmosphere at model initialization called the analysis. Two consecutive days with strong marine layer influence are selected as in 11 and 12 of June 2015 to analyze the improvement of 3DVAR data assimilation during model initialization on simulated GHI and meteorological parameters.

The forecasted GHI from WRF and data assimilation experiments are validated against SolarAnywhere (SAW) gridded data (Figure 4). The GHI biases over the southern California coast are significantly less in the WRF-3DVAR forecast, especially over San Diego County. The GHI biases are reduced by 100-200 W m^{-2} during the morning hours and up to 400-500 W m^{-2} during the noon hours in WRF-3DVAR as compared to WRF simulation. It indicates that data assimilation promotes marine layer clouds over the coastal and inland valley regions. However, GHI biases are still present during the early morning hours over regions with terrain heights greater than 350-400 m above mean sea level. This is likely a result of the model simulated inversion base heights being comparatively lower than the observation.

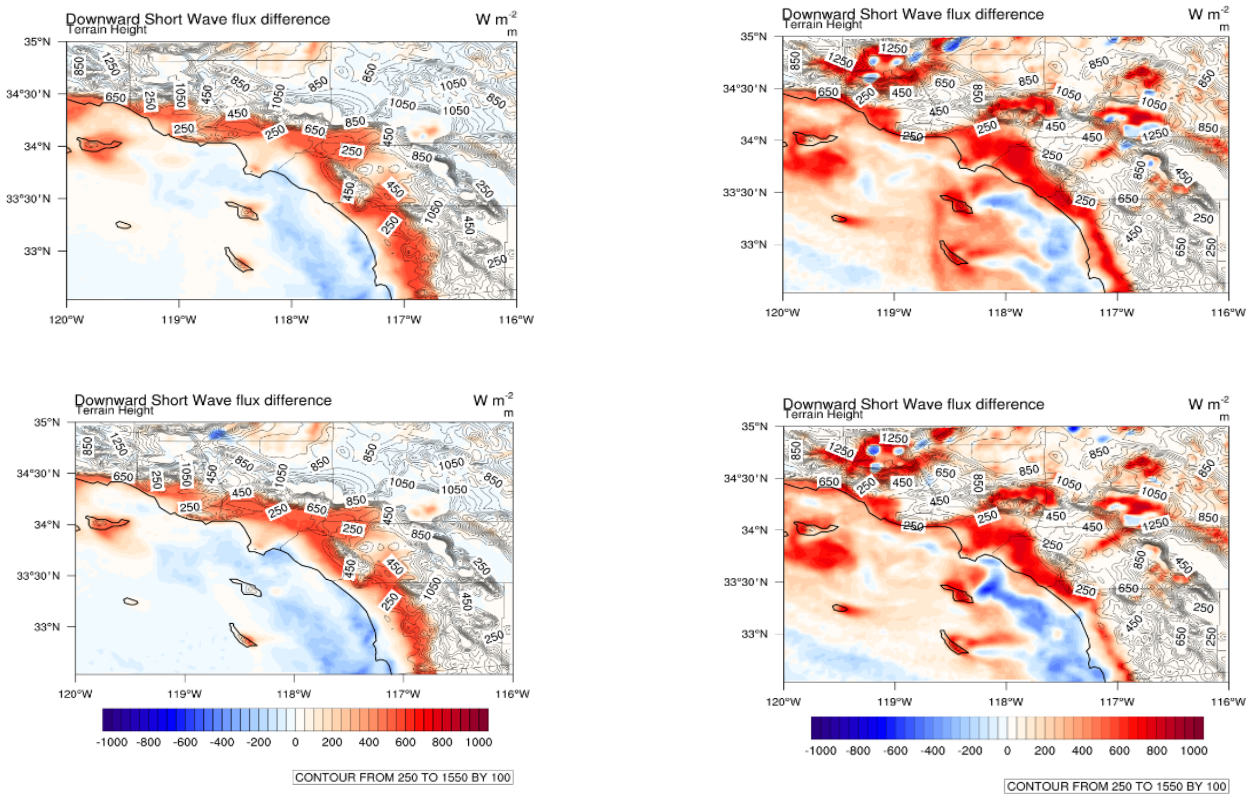

Figure 4: Spatial Biases in GHI between model simulations and SolarAnywhere (Model – SolarAnywhere) at 1600 UTC (left panel) and 2000 UTC (right panel) on 12 June 2015 for (top) WRF and (bottom) WRF-3DVAR data assimilation simulations.

3.5 Operational reliability

Like with any operational product that is provided in a time sensitive production environment, one of the key success metrics is the reliable delivery. In this specific case the distribution system operators relied on the timely solar forecast delivery as input to net load forecasting.

The original WRF forecasts were delivered on time 99% of the time (4 failures in one year). Failures occurred when the WRF forecast crashed presumably due to numerical stability issues in certain meteorological conditions. After the implementation of a redundant forecast delivery system that provides persistence forecasts from the previous day in case of a failure of the WRF run, the forecast were successfully delivered 100% of the time since January 2016.

4 Net Load Forecasting and Solar Impacts on Net Load Variability

4.1 Motivation

Variable rooftop solar generation changes the variability of net load time series and adds uncertainty in forecasts of power demand at the substation level. Especially for high solar penetration levels, the variability in solar power production propagates into the load profile and increases the error of net load forecasts during the daytime. Uncertainties in electric loads need to be compensated by operating reserves or ancillary generation, which increase the overall costs for utilities, customers, system operators, and other market participants. Short-term load forecasts play a key role in mitigating the uncertainty of loads and are essential to decrease the costs of electric grid operation.

4.2 Machine learning models and image inputs

The forecasts are produced using Artificial Neural Networks (ANN) and Support Vector Regression (SVR). ANN and SVR are popular stochastic-learning tools for pattern recognition, data classification and regression, and have proven to be useful for non-linear input/output mapping

A key input for intra-hour solar forecast is expected to be the information retrieved from sky images, as cloud cover information are critical for determining short term solar ramps. An efficient image-processing algorithm translates the sky images into numerical image features (Figure 5). These image features are used as inputs to the multi-layer stochastic learning forecast engine. The image-processing algorithm was applied to a UC San Diego Sky Imager (USI) located in Feeders A and B to create a database of sky image features. No sky imager data was used at the other 66 feeders.

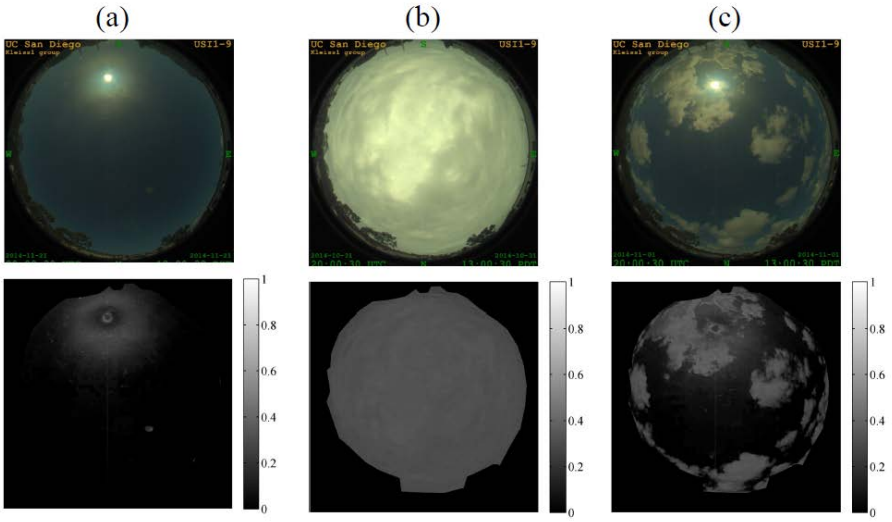

Figure 5: Examples of original images (top row) and normalized red blue ratio (nRBR) images (bottom row) recorded at Feeder B, which are returned from the image-processing algorithm. The gray scales indicate the nRBR magnitudes in each image.

4.3 Short-term forecasts

ANN and SVR short-term forecast packages were implemented for 10-, 20-, and 30-minute forecast horizons with 10-minute resolution. Forecasts for four representative feeders are presented in Table 1, while results for all 68 substations are presented in the Appendix of the Task report.

The comparison between sky-image enhanced forecasts and baseline forecasts in terms of MAE and rRMSE shows that sky imagers (Im-ex) reduce forecast errors on average by 4% to 5% over the baseline forecasts. The overall solar penetration levels at both feeders are still very low (2.4% for Feeder A, and 5.8% for Feeder B). Therefore, Im-ex forecasts only achieve marginal improvements in term of rRMSE for these two feeders. The benefits of Im-ex inputs are expected to increase for feeders with higher level of solar penetration.

Table 1: MAE and rRMSE (daytime only) for reference persistence forecasts, baseline endogenous forecasts, and forecasts with image features as exogenous inputs for 10-, 20-, and 30- minute horizons. Note that only the two feeders with available sky imager data are included in this table.

		Feeder A			Feeder B		
Forecast Horizon	[min.]	10	20	30	10	20	30
Persistence	MAE	0.020	0.037	0.052	0.020	0.035	0.049
	rRMSE	0.043	0.066	0.084	0.056	0.092	0.127
ANN	MAE	0.024	0.039	0.050	0.018	0.026	0.033
	rRMSE	0.040	0.059	0.071	0.044	0.063	0.080
ANN with Im-ex	MAE	0.025	0.037	0.042	0.018	0.024	0.028
	rRMSE	0.040	0.056	0.064	0.044	0.059	0.073
SVR	MAE	0.032	0.044	0.053	0.019	0.026	0.032
	rRMSE	0.044	0.060	0.072	0.045	0.063	0.079
SVR with Im-ex	MAE	0.027	0.038	0.043	0.020	0.026	0.029
	rRMSE	0.046	0.061	0.068	0.048	0.065	0.074

Example time-series of enhanced forecasts and corresponding absolute errors are shown in Figure 6 for Feeder B for a period of 48 hours. The daytime forecasts consider image features as exogenous inputs while the nighttime forecasts use only endogenous inputs. For feeder B penetration level of 5.8%, the impact of solar variability on the net load time series can be seen in Figure 6, particularly around noon when the solar power reaches its daily maximum. The improvement achieved using stochastic models with enhancement methods over the reference persistence model is noticeable in the time series of forecast errors. The highest improvements are observed during midnight and early morning when the net load time series has a monotonous and smooth trend. During the middle of the days when exogenous inputs are available, both ANN and SVR forecasts achieve significantly lower error than the net load persistence forecasts.

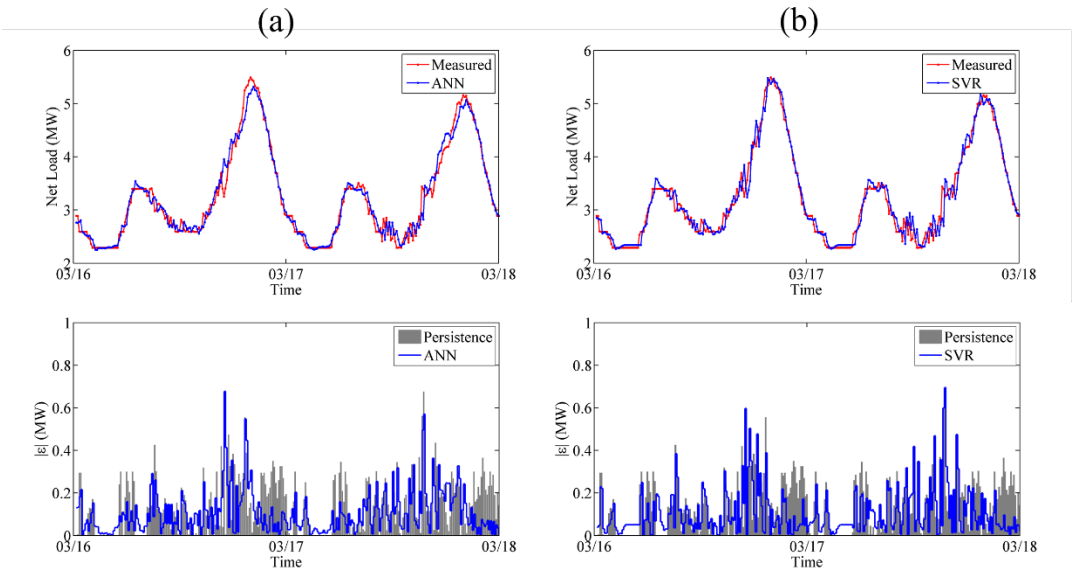

Figure 6: Sample time series of net load forecasts and absolute forecast errors (ε) for Feeder B for a period of 48h using (a) ANN and (b) SVR. The timestamps indicate midnight (00:00) PDT.

4.4 Day-ahead forecasts

Day-ahead forecasts use different exogenous data than short-term forecasts. For long forecast horizons sky images are not useful because cloud cover information derived from them is too short-lived. Instead, for day-ahead forecasts, the models use data from numerical weather prediction models. The solar irradiance and cloud cover forecasted by the North America Mesoscale Model (NAM) is used. ANN and SVR forecast models were developed and validated for the 68 substations for 1-, 2-, 3-, and 4-day forecast horizons with 1-hour resolution.

The forecast performance in terms of MAE and RMSE are presented in Table 2 for the four representative feeders. The persistence model is used as a baseline model to benchmark the implemented net load forecasting models. For all models, both the MAE and RMSE increase with the forecast horizon, regardless of the locations. For all feeders, the stochastic learning models achieve error metrics that are significantly lower than the reference persistence model, particularly for longer horizon forecasts. For example, at Feeder A, the RMSE of 2-day ahead SVR forecasts is 0.428 and the RMSE for the persistence model is 0.522, an improvement of 18%. Sample time series of forecasts and corresponding errors for 2-day forecasts (Figure 7) clearly show the improvements of the stochastic learning models over the reference persistence models, particularly during periods of large ramps.

Table 2: Net load forecasting results for 2 day forecast horizon for the four feeders.

		Persistence	ANN	SVR
MAE [-]	Feeder A	0.119	0.110	0.098
	Feeder B	0.066	0.062	0.060
	Feeder C	0.104	0.103	0.101
	Feeder D	0.118	0.102	0.106
rRMSE [-]	Feeder A	0.522	0.505	0.428
	Feeder B	0.330	0.308	0.293
	Feeder C	0.207	0.197	0.202
	Feeder D	0.225	0.196	0.204

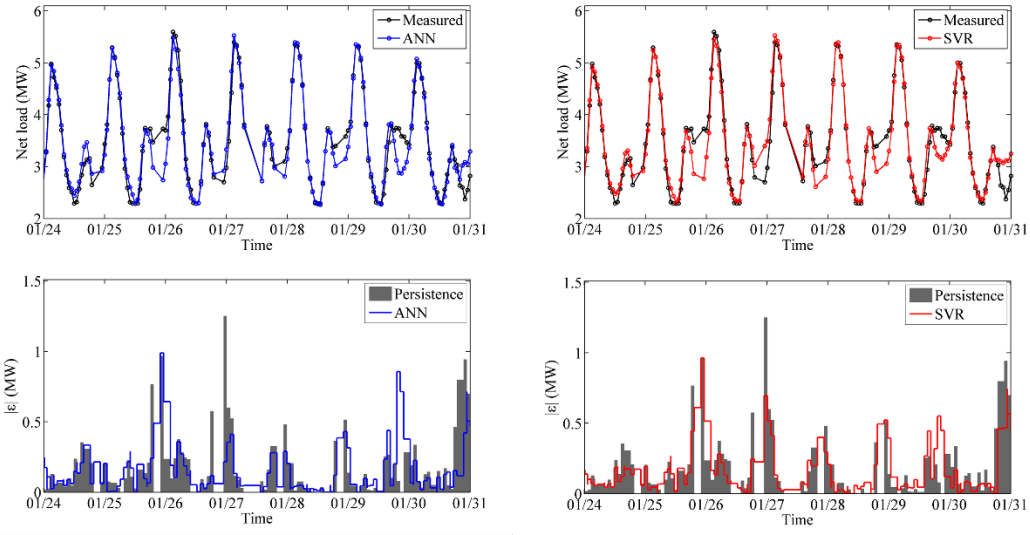

Figure 7: Sample time series of 2-day ahead net load forecasts (top row) and absolute forecast errors (bottom row) for Feeder B for a period of 1-week using ANN (left column) and SVR (right column). Persistence forecast errors are shown for reference in grey. The timestamps are in UTC.

4.5 Conclusions

To accurately forecast the net load with the influence of distributed solar production, two popular stochastic learning models were demonstrated. These net-load forecast for intra-hour and multiple day-ahead forecasts were successfully developed for the 68 substations in the SDG&E operating region. Advanced methods such as interpolation and image-processing algorithms were implemented to enhance the performance of forecasts. The models were validated using measured net load data showing that they outperform the baseline persistence model in terms of MAE and rRMSE.

The models were assembled into forecasting packages that are operational. The very small latency times allows production of operational forecasts given that robust real-time telemetry data is available from each substation. The forecast packages were implemented in real-time for 4 representative SDG&E feeders (A, B, C, and D). Operational forecasting was live for about 2 months and frequent issues with the PI server administration prevented longer operational testing. The developed models were

prepared in forecasting packages for all 68 substations. Each package includes all necessary function files, processing algorithms, and trained models to forecast the net loads. These forecasting packages are ready to be applied in real time operations.

5 Distribution Feeder Hotspots

5.1 Motivation

Distribution planners conduct power flows analysis to identify future network capacity limits for the distribution grid so that they may plan to remediate potential constraints before they occur. Network capacity limits can include thermal rating limits of current carrying conductors, and over- and under voltages exceeding ±5% of the nominal voltage. Further, voltage variations creating perceptible flicker, significant increases in load tap changer operations that may result from solar power variability, and the reach of protection devices to identify and isolate faults can also be considered when assessing network capacity limits. Increasing existing capacity limits can lead to substantial network investment for a utility.

Moreover, a considerable lead time for the project may be required so that the thermal limit is not reached before the completion of the project. Consequently, identifying future capacity limits in the distribution grid can be helpful in terms of understanding the cost and time for remediation if and when the need arises. In this section, hotspots arising with increasing distributed PV penetrations are identified with the aid of power flow analysis tools.

5.2 Distribution feeders and validation

San Diego Gas and Electric (SDG&E) provided 14 distribution feeder models suitable for power flow applications (Table 3). The models included the electrical connectivity of conductors, capacitors, voltage regulators, generators and load buses. Further, SDG&E provided a conductor database that described the positive sequence impedance of each conductor within the distribution feeder models. The 14 SDG&E distribution feeders were selected for the purpose of identifying distribution hotspots requiring network augmentations due to growth of solar PV generation. Feeders 12, 13, and 14 were classified as rural, and the remaining feeders as urban.

SDG&E provided load flow results for each distribution feeder to assist in the model validation process. These load flow results were compared to those obtained in OpenDSS to highlight and correct any potential model inaccuracies arising from the process of importing the electrical models into OpenDSS. The majority of the feeders had a very small voltage error (less than 0.005 Vpu) as a result of the model validation process.

Table 3: Distribution feeder properties. The maximum number for each category / row is in bold.

Feeder ID	1	2	3	4	5	6	7	8	9	10	11	12	13	14
Feeder length (km)	53	58	41	45	52	55	49	56	45	51	40	35	52	**115**
# Supply Transformers	298	312	285	243	416	324	212	139	260	376	322	281	276	**649**
Peak Load (MVA)	8.0	9.7	9.5	5.9	10.8	13.2	9.8	8.8	8.0	**13.6**	8.4	4.9	3.9	6.3
# Capacitors / Rated Reactive Power (MVar)	1/ 1.2	1/ 1.2	3/ 1.2, 0.8, 1.2	1/ 1.2	1/ 1.2	1/ 1.2	**(3)*/** 1.2, 1.2, 1.2	2/ 1.2, 1.2	1/ 1.2	4/ 1.2, 1.2, 1.2, 1.2	(2)*/ 1.2, 1.2	(2)*/ 1.2, 1.2	(1)*/ 1.2	(1)*/ 1.2
# Substation Transformers and Voltage Regulators	1	1	1	1	1	1	1	1	1	1	1	**2**	**2**	**2**
# PV systems	180	105	106	83	95	62	69	147	66	71	340	364	104	**387**
Peak PV output (MW_{AC})	1.9	1.1	0.7	0.8	0.9	0.8	0.8	1.9	1.1	1.3	**5.1**	1.3	2.7	2.4
2015 PV Penetration Level[1] (%)	24	12	7	13	8	6	8	22	14	9	60	51	**71**	38
Capacity (MW) of large PV systems (>0.5 MW)	0	0	0	0	0	0	0	0	0	0	0	0	**1.14, & 0.86**	0
Substation set-point voltage (pu)	**1.02**	**1.02**	**1.02**	**1.02**	**1.02**	**1.02**	**1.02**	**1.02**	**1.02**	**1.02**	1.01	0.98	0.99	1.01

5.3 Feeder hotspot methodology

5.3.1 Hot spot definition

Sections of each distribution feeder that are most affected by high PV penetration are identified. A feeder hotspot along a distribution feeder is defined by:

(1) an over- and under-voltage at a node that exceeds ±5% of a nominal 12 kV, or
(2) a steady-state power flow that exceeds a thermal rating of a conductor.

Load tap changer operations and the maximum voltage variability along a distribution feeder associated with the lowest PV penetration level that creates a feeder hotspot are also quantified. Voltage variability is defined as voltage fluctuations measured at 30-sec time steps along a distribution feeder that exceed 2%, a threshold that may prompt an investigation into the customer impacts (e.g., perceptibility of flicker).

---

* In the simulations that follow these capacitors are taken out of service to accommodate increasing levels of PV penetration.

1 The PV Penetration level is defined in Section 2.

Hosting capacity is defined by the maximum amount of PV generation that a feeder can accommodate before feeder hotspots along the feeder occur. In what follows feeder hotspots that arise from a range of PV penetrations are used to infer the associated hosting capacity.

5.3.2 Solar PV and Load Input Data

To consider the impact of high PV penetration levels on each of the feeders, the rated PV output for each existing and virtual (only for feeders 11-14) PV unit is scaled equally. To realistically consider the impact of PV generation variability arising from moving cloud cover on each the distribution feeders, PV generation profiles for each PV unit are simulated using available sky images. More specifically, sky images taken every 30 seconds were used to produce unique generation profiles at each of the PV sites on each distribution feeder.

For four feeders, the 15 min resolution load demand time series was available from SDG&E. For the remaining feeders, data from one of the four feeders was used, but rescaled using the maximum power consumed by all loads along a given feeder P_{load_peak}.

5.4 Sample results for feeder 3

Sample results for one feeder are presented here, while the task report contains similar sections for each feeder. Feeder 3 is operated at a nominal 12 kV, is characterized as urban with a length of 41 km, carries a peak load of 9.51 MVA, and connects 285 supply transformers that step the voltage down to a lower voltage from which residential and commercial loads are supplied. Further, 106 PV units are connected to the secondary side of the supply transformers, the majority of which are located on residential rooftops. In Figure 8 the location and size of PV units included in the model of feeder 3 are depicted by circles.

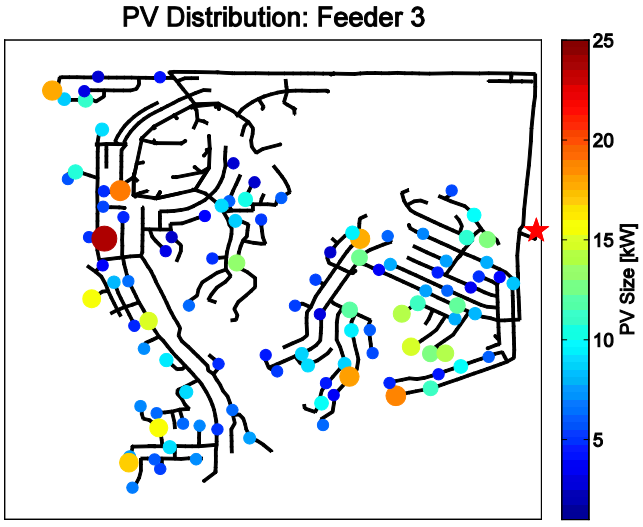

Figure 8: PV distribution map with circles proportional to the size of the system. The star indicates the distribution substation where the on-load tap changing transformer is located.

In Figure 9 geo-schematic single line diagrams of feeder 3 are presented with feeder hotspots corresponding to various PV penetration levels, where hotspots along an edge arise due to thermal limits of electrical conductors and hotspots at a node arise due to voltages exceeding ±5% of the nominal 12 kV.

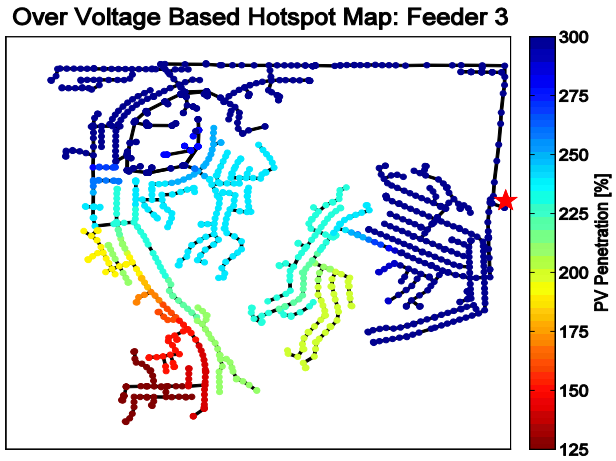

Figure 9: Hotspot map for feeder 3. The star indicates the distribution substation where the on-load tap changing transformer is located, and each node represents a device or an interconnection point along the 12kV feeder. The color bar indicates PV penetration levels that correspond to a thermal over-load (line color) and/or voltage exceedance.

The feeder can accommodate PV penetrations below 125% without the need for network augmentation to mitigate thermal limits of the conductors and/or voltage violations exceeding ±5% of the nominal 12kV. A significant proportion of the feeder can accommodate PV penetrations up to or possibly above 300%. Both voltage violations and thermal capacity constraints contributed to the observed feeder hotspots in Figure 9. That is, in the simulation results a number of conductors were insufficiently rated for PV penetrations up to 300%. PV penetrations of more than 300% were not examined. Hotspots at 300% could tolerate higher penetration levels. Further, the hotspots associated with a PV penetration level of 125% were located towards the end of the distribution feeder.

Feeder 3 includes two 1.2 MVar capacitors with assumed 60 kVAr steps and a single 0.789 MVar capacitor with assumed 39.45 kVar steps located 2.8 km, 4.5 km, and 3.4 km, respectively, from the distribution substation. Each capacitor is controlled for the purpose of improving voltages along the 12kV feeder. Further, feeder 3 includes an on-load tap changing transformer at the distribution substation with a set point of 1.02Vpu that is also operated with the purpose of improving voltages along the 12kV feeder. All of these voltage regulation devices are active in the simulations. Figure 10 (left) shows a small increase in the number of daily tap operations for PV penetrations above 150%.

Figure 10 (right) shows an increase in the number of switching events as PV penetration increases. The number of switching events increases as PV penetration increases because the capacitor reduces reactive power output as PV generation increases, and increases reactive power output as PV generation decreases and the load increases in the evening.

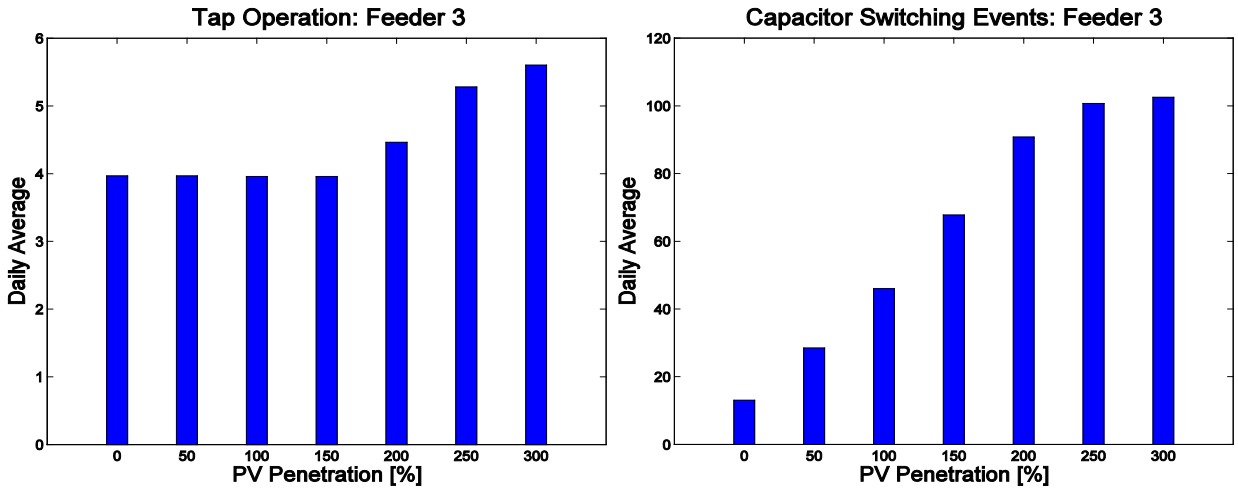

Figure 10: Left, the average number of daily tap operations corresponding to the on-load tap changing transformer located at the distribution substation. Right, the daily average switching events for the capacitor.

5.5 Summary of the feeder hotspot analysis for 14 distribution feeders

Table 4 summarizes the feeder hotspots arising from high PV penetration levels based on OpenDSS simulation results for each of the 14 SDG&E feeders. Significant increases in PV penetration levels across all of the 14 feeders is feasible without the need for network augmentation. Further, the increase in PV penetration levels varied from feeder to feeder, as it was dependent on the feeder topology.

Feeder hotspots associated with the lowest PV penetration level were typically observed towards the end of a distribution feeder and/or along small branches of the feeder that did not carry the trunk sectional load. In all cases PV units were located at these respective hotspots. In Table 4 the conductor rating at the location of each feeder hotspot together with the trunk sectional rating of the feeder is a helpful proxy in determining conductor impedances that may contribute to voltage-based hotspots. Consequently, PV generation sites closer to the trunk sectional load where the conductor has been sufficiently rated would improve the hosting capacity in most cases.

Table 4: Summary of the feeder hotspots for each of 14 SDG&E feeders. The maximum entries in each category / row are in bold.

Feeder ID	Existing PV Penetration [2]	Lowest PV Penetration Coinciding with a Hotspot	Max Voltage Variability at Lowest PV Penetration Coinciding with a Hotspot	Daily Average Transformer Tap Changes at 0% PV Penetration	Daily Average Transformer Tap Changes at 300% PV Penetration	Rating of conductor/s creating a feeder hotspot at lowest PV penetration	Trunk Section Rating
1	23.5%	280%	2.0%	3.7	3.7	130 A	700 A
2	11.6%	250%	4.2%	4.5	4.5	500 A[3]	580 A
3	6.9%	125%	3.0%	4.0	5.6	180 A	700 A
4	13.1%	200%	2.2%	1.6	2.8	180 A	770 A
5	8.4%	150%	2.4%	4.7	4.2	130 A	770 A
6	6.1%	125%	3.2%	6.0	8.0	115 A	700 A
7	8.3%	125%	2.4%	1.0	11	180 A	580 A
8	21.9%	150%	3.2%	11	9.0	130 A	700 A
9	13.8%	100%	1.7%	2.7	2.2	130 A	770 A
10	9.2%	100%	4.7%	9.2	9.7	180 A	580 A
11	60.4%	100%	2.6%	2.0	9.5	15 A	520 A
12	51.4%	260%	1.5%	3.5	10	180 A[4]	520 A
13	71.0%	250%	3.0%	18	44	130 A	520 A
14	38.0%	100%	5.2%	31	78	180 A	770 A

2 Feeders 11-14 have some addition artificial PV deployments.

3 Thermal hotspot.

4 Thermal hotspot.

6 Allocation of Battery Energy Storage Systems in Distribution Networks Considering High PV Penetration

6.1 Introduction

Planning and managing the electric distribution system is becoming more challenging due in part to the emergence of widespread distributed renewable generation. Considering that in the near future solar PV systems will likely saturate in low-voltage distribution grids, grid reinforcement may be required to keep the energy network running without operational issues and allow further increase in PV penetration.

In a low-voltage distribution grid with high amounts of grid-connected solar PV in California, high generation and low load conditions are expected nearly on a daily basis when there is plenty of sunshine during midday but not many customers at home consuming electricity. Such conditions may result in overvoltages and/or overload transformers or current carrying cables. Fluctuating electrical power during partial cloud cover may result in increased tap changes to compensate the resulting voltage fluctuations. Yet during periods of thick cloud cover or rain, high power flows from the substation need to replace the missing local PV generation. In the absence of on-site storage, such events may be responsible for peak feeder loading. This dependency on weather conditions often will prohibit capacity deferral cost savings through PV alone.

As a result, increased penetration of intermittent distributed power generation sources creates a great potential for battery energy storage systems (BESS). This work fills the gap in understanding how BESS sizing and siting maximize the benefit of such systems. To achieve this goal a genetic algorithm (GA)-based multi-layer multi-objective optimization model allocates BESS (storage sizing, storage siting) in a distribution feeder and operates the BESS according to a storage dispatch strategy obtained from a linear programming (LP) routine (storage operation).

6.2 Optimization objective function

The goal is to optimally size and site BESS within a distribution network under a certain penetration of distributed PV. The optimum BESS configuration is determined by controlling the three decision variables: the total BESS capacity in the feeder, the size of each BESS, and the installation node of each BESS. The term *BESS configuration* is used herein to mean the set of these three decision variables.

The multi-objective optimization, given in Eq. 1, is formulated as a weighted sum method.

$$max\ \{[n_1\overline{L}_{\Delta E} + n_2\overline{V}_{dev} + n_3\overline{T}] \cdot \lambda_{cost}\} \qquad 1$$

The optimization routine aims to maximize this “fitness value” of a BESS configuration. The terms given within the parenthesis represent various value streams for the utility. $\overline{L}_{\Delta E}$ is the energy loss reduction achieved through BESS utilization, $\overline{V}_{dev}$ is the reduction in voltage deviations at the most-impacted

nodes within the network, $\bar{T}$ is related to the operational life expectancy of BESS, and λ_{cost} is a penalty multiplier that accounts for battery procurement and installation costs.

The terms in Eq. 1 are motivated by the fact that BESSs can shift PV generation from peak solar power generation hours to peak load hours, reducing congestion and energy loss and avoiding reverse power flows. Energy storage systems can also decrease voltage deviations caused by local PV systems by absorbing the excess generation and discharging / supporting the network when the local generation decreases (e.g. due to a moving cloud impacting several PV systems).

Excessive use of BESS to fulfill the voltage deviation and energy loss objectives can be costly by shortening the BESS lifetime. A simple battery degradation model is used to assess the impact of BESS operating strategies on BESS operational life expectancy (BESS lifetime). BESS lifetime acts as a differentiator between different BESS configurations with similar $\bar{L}_{\Delta E}$ and $\bar{V}_{dev}$ that are achieved with less impact on the battery.

A qualitative BESS cost penalty model is applied that combines BESS capital, installation and land-of-use, and economies of scale concepts into a single cost penalty multiplier, λ_{cost}, that penalizes larger capacity BESS (although partially mediated by reduced costs per unit) and more dispersed BESS installations in the network. For each additional BESS installation site, the utility will incur additional fixed expenses (e.g. real estate, permitting, electrical interconnection). This relation is represented as increasing costs as more sites are used.

6.3 Simulation setup

6.3.1 Power flow simulations

Quasi-static time series power flow simulations are performed using OpenDSS, an electric power distribution system simulator. The IEEE 8500-Node test feeder with balanced 120V secondary loads on the service transformers is chosen as the benchmarking circuit. This circuit is a radial distribution feeder with multiple feeder regulators and capacitors and is a suitable test feeder to assess the performance of the proposed algorithm as it is similar to a large feeder with many typical elements found in a residential distribution feeder. Another case study is conducted for a distribution feeder in the SDG&E service area (feeder E).

The PV generation fleet is assumed to be composed of distributed rooftop systems. In the IEEE8500 feeder, for each level of PV penetration, PV systems are sited randomly among the load points of the circuit until the desired penetration is reached. Each system is specified to have a capacity equal to the peak demand of that bus. For feeder E, existing PV systems are kept in place while additional systems are added to the circuit at random locations. Unlike for the IEEE8500 feeder case, the PV system locations are fixed and only the sizing for all PV systems is scaled to match the desired PV penetration.

6.3.2 BESS operation

Batteries are chosen such that the kW rating of each BESS matches its kWh capacity (i.e. power to energy ratio of 1). Battery dispatch for each system is determined by a linear programming (LP) routine that minimizes the daily peak demand at the substation. The LP routine receives perfect solar PV power and load forecasts as input and sets a net load reduction target. Since reverse power flow can cause a variety of power quality and protection issues, the LP routine is adjusted. When there is a reverse power flow from the circuit to the slack bus, battery dispatch is updated to force the battery to charge for the duration of excess generation.

6.3.3 Optimization method: Genetic Algorithms

Given the nonlinear nature of power flow analysis and fairly large and unknown solution space formed by the three decision variables and the battery dispatching strategy, genetic algorithms (GA) are a viable global search algorithm option for this problem. The general methodology in a typical GA is presented in Figure 11. After completing power flow simulations for each BESS configuration (*individual*) in the current set of simulations (current *generation*), the individuals are sorted with respect to their achieved fitness values. The best few individuals (*elite*) are directly passed to the next set of simulations (next *generation*) through *elitism*. Elitism allows the optimization routine to keep the characteristics of good solutions.

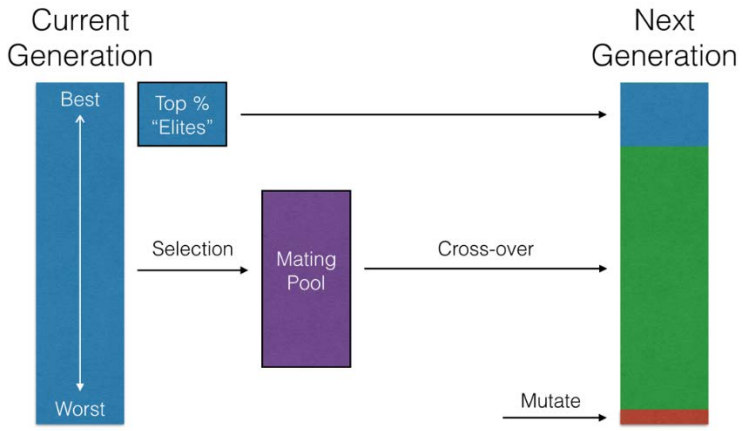

Figure 11. Each new generation is created through Genetic Algorithm (GA) operators: selection, cross-over and mutation. The next generation includes best individual(s) from the current generation (through elitism) and newly created individuals as a result of GA operators.

6.4 Results for a sample day

Typical daily BESS operation is shown in Figure 12a and b. The BESS smooth the ramps with short discharge cycles between 9 am and 1 pm. Without BESS reverse power flow through the slack bus would have occurred at 11:45 am and at 1 pm. Reverse power flow is mitigated by sending steep charging

signals at these time steps. Prior to 6pm the BESS are fully charged and after 6pm are discharged to shave peak demand.

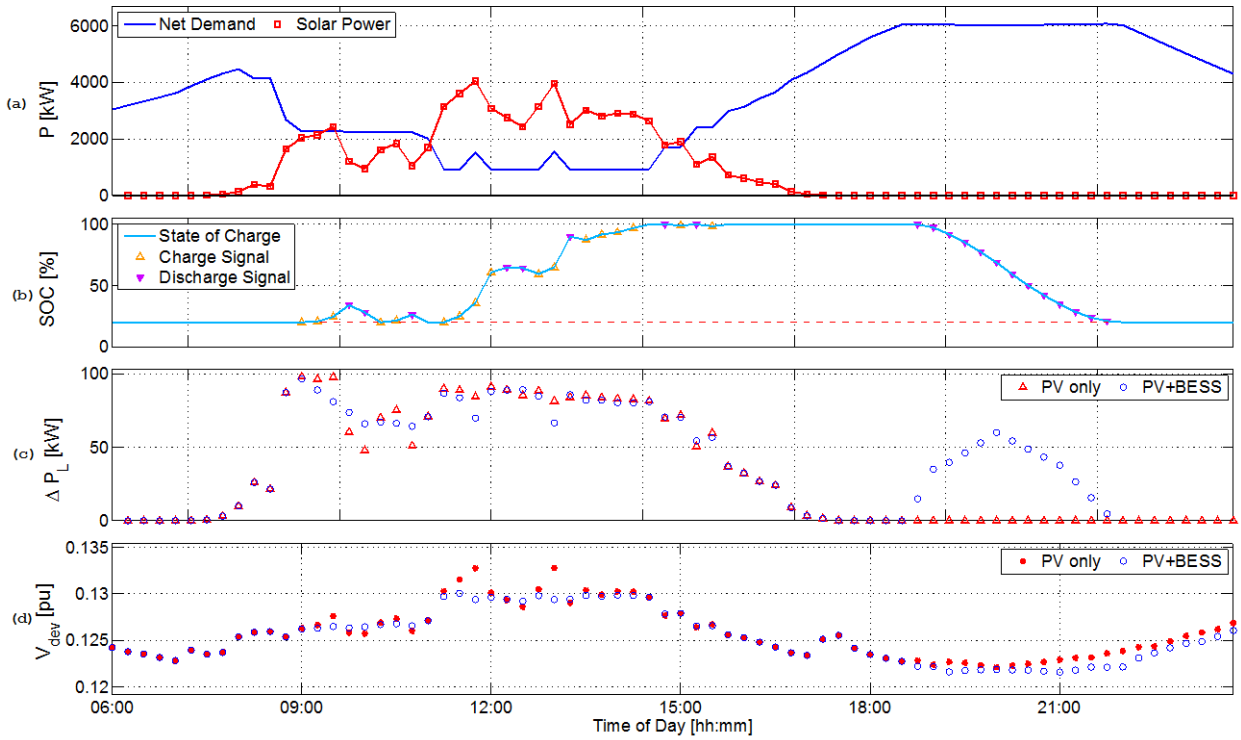

Figure 12. Overview of a typical daily simulation. The case shown is 50% PV penetration on a partly cloudy day for the IEEE 8500 test feeder. (a) aggregate net demand (Load minus PV minus BESS) and solar power generation. (b) cumulative BESS state of charge and charging & discharging signals. (c) Energy loss reduction compared to the reference case (no PV). (d) voltage deviation among critical nodes with respect to 1pu.

From each power flow simulation, the benefit terms of the objective function in Eq. 1 are computed. Figure 12c shows the impact of PV ($\Delta P_{L,i}^{pv}$) and PV+BESS ($\Delta P_{L,i}^{pv+bess}$) operation on energy loss reduction for each time step i. During hours of PV generation, PV systems decrease energy loss since energy demand is satisfied through locally-generated power. The BESS minimally increase energy loss because they charge, thereby adding to the feeder load. During the evening peak, the BESS dispatch and reduce energy loss significantly.

Figure 12d shows the impact of PV ($V_{dev,i}^{pv}$) and PV+BESS ($V_{dev,i}^{pv+bess}$) operation on voltage deviation. BESS dispatch reduces net demand fluctuations caused by PV generation stabilizing the local voltage. BESS also support the voltage by injecting power locally during peak consumption. While the largest total reduction in voltage deviation occurs during the evening peak load, the largest temporary reduction occurs during peak solar generation.

6.5 Sample BESS siting and sizing results

The optimization output of sized and siting of BESS units are shown in Figure 13 on a distribution feeder map.

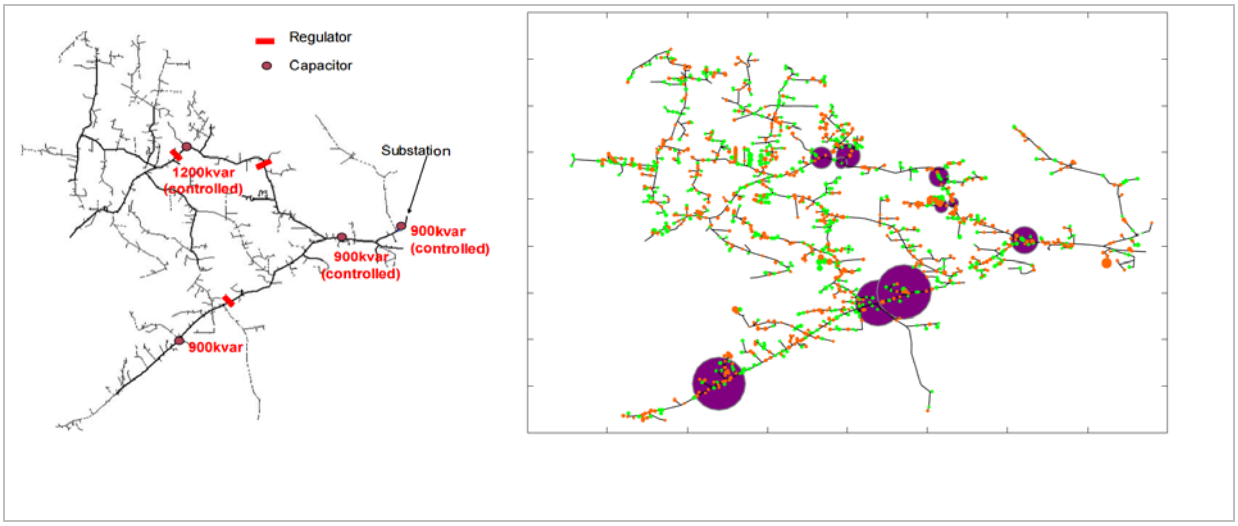

Figure 13. IEEE8500 test feeder one-line diagram and siting results of a representative simulation with 50% PV penetration for a partly cloudy day) (Left) One-line of IEEE8500 test feeder primary lines with regulator and capacitor locations marked. (Right) One-line of the optimal BESS solution. Locations of proposed BESS units are marked with purple dots. Orange dots show loads with PV and green dots show load points without PV. Each dot is sized with respect to the capacity of the component it is representing.

The robustness of the algorithm is demonstrated in Figure 14. Six different regions are marked with red circles. These circles identify regions where the optimization consistently sited one or several BESS. The variation of BESS siting within these marked regions are natural and expected given the heuristic nature of the optimization routine and insignificant impact of re-locating certain BESS to their immediate neighboring nodes. However, identifying such regions with a degree of confidence is important to validate the methodology. Considering that there are 1621 permissible nodes on the lines for the feeder E, convergence to several distinct regions demonstrates that the optimization is consistent and suggests that the final result is a global optimum. Figure 14 proofs that the optimization routine correctly implements the methodology and successfully recommends preferred locations for BESS to achieve utility objectives.

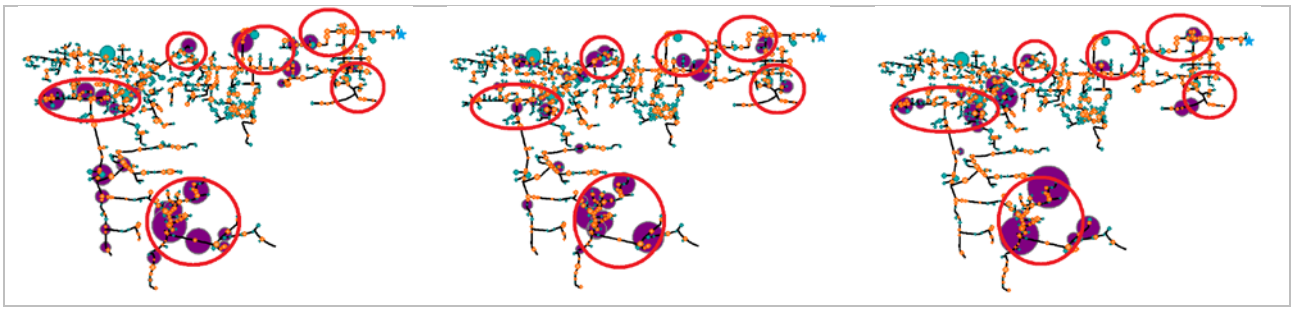

Figure 14. Simulation convergence for three simulation runs with the same settings. Regions that are chosen in all three runs for BESS installations are marked with red circles. The substation location for the feeder is indicated with a blue star on the top right. Results are for 75% PV penetration for feeder E for a day with clear morning and afternoon and partial cloud cover in the evening

6.6 Siting application notes

With regard to siting, there are three types of energy storage that are currently being installed in California, behind the meter, community energy storage, and bulk utility energy storage. Community energy storage is currently being installed and tested by all three major IOUs in California, and generally range in size from 20 – 100 kW. Community energy storage is generally installed directly within existing utility distribution easements and franchise right of way, and not in the substations. Community energy storage is generally connected directly to distribution primary and secondary power lines. This report focuses primarily on siting of community energy storage systems along the distribution system to improve overall distribution system performance and reliability.

The optimization routine will find the best location and size based on electrical system performance, however it is very probable that siting constraints, such as environmental, geographic, and others could make some locations infeasible. Therefore the permissible nodes for BESS installation points within the network can be tailored to account for any siting restrictions due to technical, environmental or human factors. The optimization routine accepts any subset of the network for BESS siting consideration and returns the feasible siting options and proper BESS sizing for the given permissible node set, demand and solar profiles, and the level of PV penetration in the circuit.

The optimization routine often places several BESSs in close proximity of each other. Such close placement is probably practically suboptimal and can be prevented by setting only discontinuous / isolated points within the network as possible BESS locations. If inter-connected permissible node sets are preferred, either closely placed systems can be aggregated into single systems as a post-processing step, or a minimum distance condition between each BESS can be imposed during the simulations. The MATLAB algorithms are provided at www.calsolarresearch.org.

7 Energy Storage Systems Optimization and Dispatch

7.1 Motivation

More renewable energy generation leads to inherent variability in energy production. In addition, renewables, especially solar PV, lack the rotational inertia of conventional generation and therefore are not able to stabilize and maintain synchronous operation of the system. This combination of increased variability and lack of physical inertia could result in increasing instability and poorly damped oscillations in AC frequency and power. These instabilities can lead to increased wear and tear on the electrical grid, increased outages, and even electrical equipment damage.

More generally, instabilities on the grid can be caused by generation loss, topology, load changes and increased penetration of renewable power sources. An example of such power oscillations is shown in Figure 15, where oscillations in real power were observed in the 12 kV connections at the University of California, San Diego during a particular load switching. In general, electric power systems are subjected to power oscillations due to the inherent inertia of generators and loads. Such power oscillations are typically in the 0.2-3 Hz range, depending on the size of the (micro)grid and the characteristics of the interconnected power system. Additionally, measurements on distribution networks indicate harmonic and non-sinusoidal power flow and, especially in microgrids, they are showing that overall power quality may not meet standards. The electric power industry is beginning to observe power grid dynamic behavior through abundant Phasor Measurement Units (PMUs). For example, five relay based PMUs and dedicated PMU devices have been operational on the microgrid of UCSD. The distributed nature of the PMUs provides source measurement required to compute the angle difference across the entire campus.

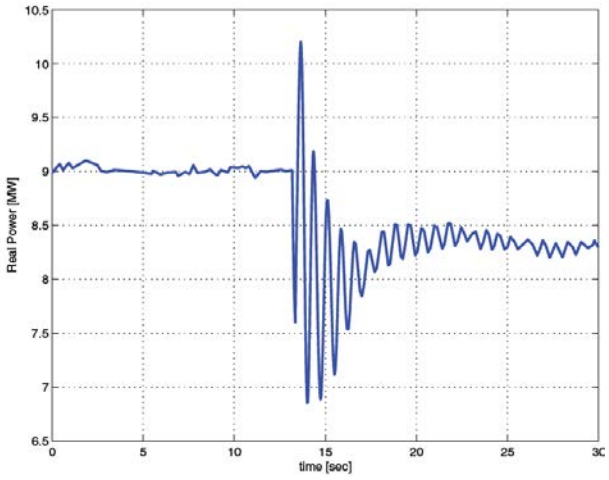

Figure 15: Measured real power oscillation on the main 3 phase interconnect of the UCSD microgrid during a step-wise load demand change

7.2 Objectives

The objective of this subtask was to develop, operationalize, and demonstrate an energy storage dispatch control scheme that can mitigate power fluctuations. The first part of this task was to show how three phase real power measurements can be used to formulate a low order dynamic model of an electric (micro)grid by observing power oscillations due to a load or generation disturbance. The second part was to apply this model to develop an energy storage dispatch control scheme to mitigate these disturbances.

7.3 Identifying a low order model

A line switching, a load switching, a fault, or anything else could be the disturbance that causes power oscillations. As these disturbances are typically step disturbances, explicit information on the shape of the input signal that caused the power oscillation will be beneficial, especially when multiple step signals occur in close proximity in time. Explicit use of input and observed output signals via a system identification procedure will improve the quality of the models that capture the power oscillations.

The low order model of the power oscillations is formulated in the format of a discrete-time state space model that is a set of coupled first order difference equations of the format

$$x(t+1) = Ax(t) + Bu(t)$$
$$y(t) = Cx(t),$$

where the output $y(t)$ reflects the time t synchronized power flow measurements produced by a PMU, $u(t)$ is the step-wise input signal, and $x(t)$ is the internal state of the power flow. It is important to realize that the size of the state $x(t)$, and, thus, the state matrix A, input matrix B and output matrix C are kept as small as possible (known as a low order model) to facilitate simplified models for which control design and hardware-in-the-loop simulation will be possible. A low order state space model that accurately captures frequency and damping of the power oscillations can be estimated via a realization algorithm that uses transient effects as will be shown in Section 7.6.

7.4 Energy storage dispatch control scheme

Once the model is available, it can be used to formulate and demonstrate an energy storage dispatch control scheme by using the model to develop a linear control algorithm indicated by $K(q)$ that can minimize the effect of an external disturbance $v(t)$ in the state space model

$$x(t+1) = Ax(t) + B_i u_i(t)$$
$$y(t) = Cx(t) + v(t)$$

and the feedback controller

$$u_i(t) = K(q)y(t),$$

where the time t synchronized power flow measurements $y(t)$ produced by a PMU are now fed back into a control algorithm $K(q)$ to feed actual inverter input $u_i(t)$ connected to the same grid on which earlier step-wise disturbances *v(t)* were present (Figure 16).

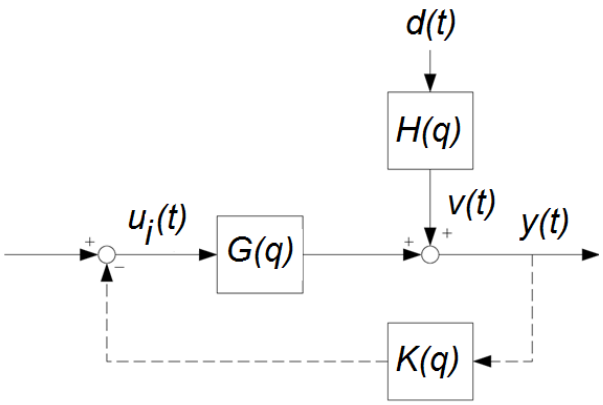

Figure 16: Schematic diagram of feedback control configuration implemented in the testbed for power oscillation control. The model G(q) represents the to-be-controlled grid dynamics with the grid-tied inverter, H(q) is the dynamic model of the step-wise disturbance d(t) affecting the power flow measurement y(t) via the output disturbance v(t) and K(q) is the control algorithm producing the control signal u_i(t) to the grid-tide inverter.

It should be noted that the input matrix B has changed to B_i as the inverter and its input $u_i(t)$ may not be collocated with the step wise disturbances used to measure the power flow dynamics. However, the location of the PMUs producing the real-power data and the dynamics of the grid remains unaltered, allowing us to use the same state matrix A and output matrix C for the control design. As a result, the to-be-controlled grid dynamics are now described by

$$G(q) = C(qI - A)^{-1}B_i$$

that is used for the design of the controller $K(q)$. The control algorithm $K(q)$ used to mitigate power oscillation disturbances consists of a series of linear filters

$$K(q) = H(q)S(q)L(q).$$

$L(q)$ is a low pass filter that ensures only inverter control signals $u_i(t)$ below a certain frequency are sent to the inverter. The high pass filter $H(q)$ ensures that the controller only reacts to changes or oscillations in power fluctuations $y(t)$ and not to steady state changes. Last, $S(q)$ is the stabilizing filter that ensure the feedback connection of the state space model and the feedback controller is stable and improves the damping of the uncontrolled electric grid system.

7.5 Lab experimental setup

An experimental setup is required to verify the performance of three phase real power oscillations and install a real-time damping control system. The experimental setup is used to repeat and initiate the scenario of an oscillatory three phase power disturbance similar to what could be observed on the real power grid. A Grid-Tied Inverter (GTI) synchronizes the AC output of the PV panels with the grid. According to such a circuit topology, an experimental setup is built as shown in Figure 17.

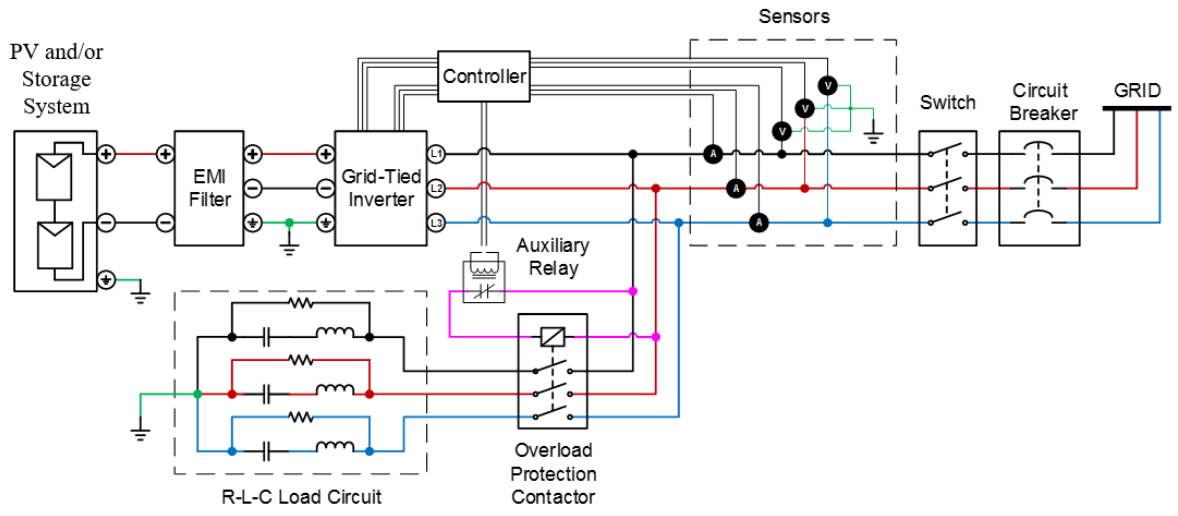

Figure 17: Diagram of experimental setup with DC power supply simulating the PV power source, an EMI filter to reduce AC ground coupling and a Grid-Tied Inverter (GTI) to provide 3 phase AC power.

The three-phase AC voltage and current signal of the grid-tied inverter and PMU sensors is measured, conditioned, and sent into the controller that computes real-time power oscillation in the circuit. The controller can also send out control signals via a signal conditioning circuit to control the four quadrant power flow through the GTI. The controller also digitally switches an auxiliary relay to switch in a three phase Resistor-Inductor-Capacitor (RLC) circuit to initiate three phase power oscillations in the circuit.

7.6 Event detection from PMU signals

A disturbance event provides valuable information on the dynamic parameters of the microgrid or the larger grid. However, to study and monitor the stability of the grid, first the disturbance event must be detected. As PMUs distributed throughout a microgrid may produce multiple (noisy) data streams in excess of 30Hz sampling, automatic and real-time detection of disturbance events is a first prerequisite for the extraction of (dynamic) information from grid disturbance events.

Signal processing with recursive estimation is used to facilitate real-time detection of disturbance events (in user-specified frequency bands) by automatically adjusting the threshold levels for each PMU distributed throughout the electric grid. Once a disturbance has been detected, the event is quantified by its dynamic parameters by estimating the oscillation frequencies and damping parameters using a realization algorithm.

To illustrate the proposed event detection based on the one step ahead prediction error minimization, followed by adaptive threshold crossing of a filtered rate of change (FRoC) signal, frequency measurements from PMUs located at UCSD and distributed in the Western Electricity Coordinating Council (WECC) during May 30, 2013 from noon till 9pm are used. PMU data (Figure 18) indicate a major power disturbance event around 4pm but other small events are also present.

Based on measurements of the PMU frequency signal $F(k)$ before any power disturbances were present, the parameters of the prediction error filter are calibrated and the resulting variance of the FRoC signal is estimated. The results are depicted in Figure 18, indicating that the proposed event detection algorithm marks (in red) several events including the major event.

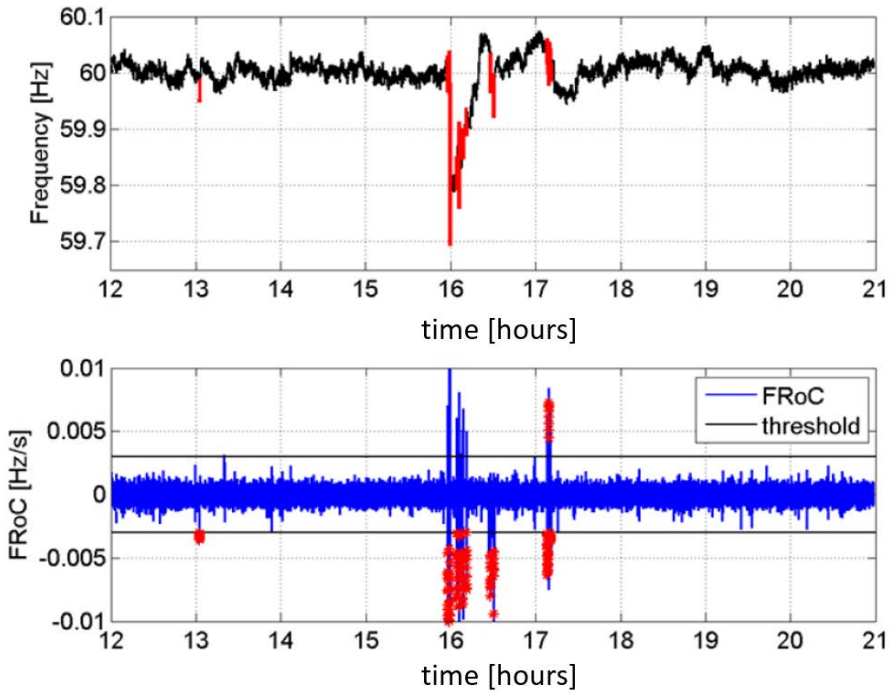

Figure 18: Measured PMU frequency data at UCSD (top) and FRoC signal with estimated threshold (bottom). The red points indicate detected events.

7.7 Event modeling using step-based realization algorithm (SBRA)

7.7.1 Characterizing power oscillation dynamics

We assume that the power oscillation is due to a step-wise change in load demand or solar power generation. The size of the load demand may not be known, but the *a priori* knowledge of the step-wise load demand can be exploited to formulate a low order state space model to model the dynamics of any observed power oscillations. In particular, the low order state space model can be realized on the basis of a real-time measurements of three phase real power oscillations to accurately model frequency and damping of the power oscillations.

7.7.2 Events created using bump tests

In the experimental verification of the real-time real power demodulation and application of the Step-Based Realization Algorithm (SBRA), power oscillations are induced by the three phase Resistor-

Inductor-Capacitor (RLC) circuit. The input $u(t)$ steps from 0 to 1 at $t = 0$. As shown in Figure 19, a third-order state space model is realized and the dynamics are captured.

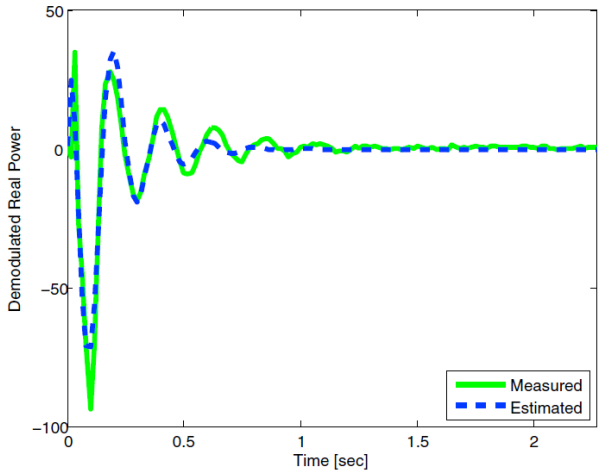

Figure 19: Comparison between measured and modeled/estimated real power oscillation. The model is a third order linear model.

7.7.3 Real power grid events

To illustrate the use of the SBRA, the time synchronized frequency measurements from three different PMUs are used to quantify a real event. The difference in dynamics between the different PMU data can be observed. The SBRA algorithm requires 10 states (5 resonance modes) to accurately capture the oscillation frequencies and their damping coefficients. With the estimated discrete-time state space model we can also re-simulate the event and provide a direct comparison with the measured time synchronized frequency measurements from the three different PMUs. Figure 20 indicates an excellent fit of the measured data.

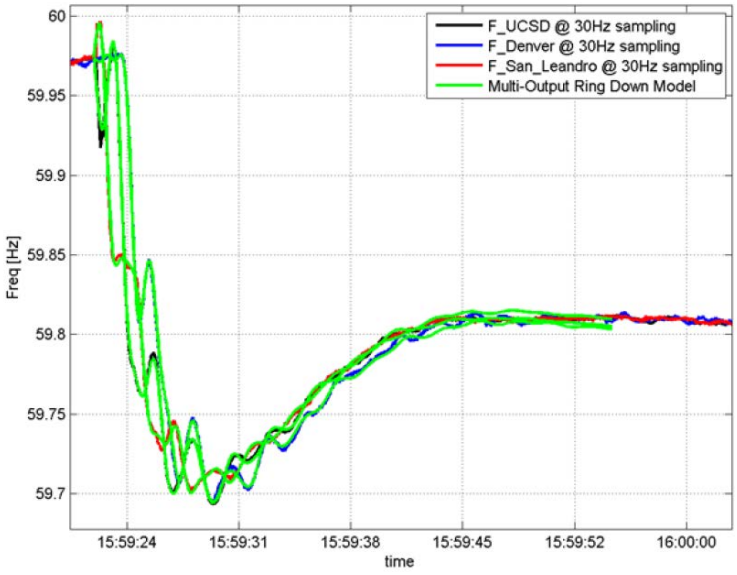

Figure 20 Comparison between PMU data and simulated data based on estimated discrete-time state space model via the SBRA algorithm for the analysis.

7.8 Conclusions and algorithm

The effectiveness of the approach illustrating both the realization algorithm and the control methodology are illustrated on the measurements obtained from a three phase RLC network where the power oscillation frequency and model order is known and used for comparison and validation of the method. The approach shows how the power oscillation frequency can be recovered from real-time measurements and reduced very effectively with the proposed control algorithm. The approach shows a close connection between modeling power flow dynamics from disturbance data, creating data-based models, and using those model for control design to mitigate electric power oscillations that exploit the fast dynamics and response time of modern inverters.

The next step in the project would have been to implement the control approach on the UCSD microgrid to demonstrate that grid fluctuations can be effectively mitigated with the proposed design. This phase of the project could not be completed due to cybersecurity issues and time constraints. Between the proposal writing and contracting and the active period of the grant, several incidents occurred on the UCSD microgrid where outside parties attempted to gain access to critical electrical infrastructure. Such access could potentially cause microgrid outages and/or damage electric components. As a result much more stringent cybersecurity policies have been put in place that essentially prohibit anything except data sharing on the UCSD microgrid. Projects such as this where network-connected hardware would take actions that manipulate power flow are no longer feasible in the current cybersecurity environment. While policies may be relaxed after increased cybersecurity is in place, the time constraints of the contract did not allow for associated delays. Therefore this part of the task had to remain incomplete and the associated funding was not consumed.

References to Task Reports

Reports Completed under this Agreement

Reports are available at http://www.calsolarresearch.org/funded-projects/112-comprehensive-grid-integration-of-solar-power-for-sdg-e

- Cost Share: ***Operations Report on 30 kW/ 30 kWh PV Integrated Energy Storage System.*** Torre, W.V. UC San Diego, Center for Energy Research. Prepared for the CA Energy Commission, Public Interest Energy Research (PIER) Program. October 2014. PDF (1MB)
- Task 2 Final Report: ***Advanced Operational Ensemble Solar Forecasting System***. Kumar, D., Wu, E., Yang, H., and Kleissl, J. UC San Diego, Center for Renewable Resource Integration and Center for Energy Research. Prepared for the CSI RD&D Program. July 2016. PDF (2MB)
- Task 3 Final Report: ***Granular Operational Net Load Forecasting.*** Chu, Y., Coimbra, C., and Pedro, H. UC San Diego, Center for Renewable Resource Integration and Center for Energy Research. Prepared for the CSI RD&D Program. April 2016. PDF (506KB). The operational forecasts can be seen at this link: http://132.239.222.136/CSI4/DayAhead_Forecasts.html
- Task 4.1 Draft Final Report: ***Distribution Feeder Hotspots***. Li, C., Ratnam, E., and Kleissl, J. UC San Diego, Center for Renewable Resource Integration and Center for Energy Research. Prepared for the CSI RD&D Program. May 2016. PDF (12MB)
- Task 4.2 Final Report: ***Allocation of Battery Energy Storage Systems in Distribution Networks Considering High PV Penetration***. Babacan, O., Torre, W., and Kleissl, J. UC San Diego, Center for Renewable Resource Integration and Center for Energy Research. Prepared for the CSI RD&D Program. January 2016. PDF (1.4MB). See zipped data file in the DATA section along with a README file explaining how to interpret the actual data.
- Task 4.3 Final Report: ***Energy Storage Systems Optimization and Dispatch***. Kleissl, J. UC San Diego, Center for Renewable Resource Integration and Center for Energy Research. Prepared for the CSI RD&D Program. October 2016. PDF (430 KB)
- Cost Share: ***Long Term Endurance Testing of Distributed Energy Storage Systems (DESS)***. Torre, W.V. UC San Diego, Center for Energy Research. Prepared for the California Energy Commission. April 2014. PDF (1.5 MB)